https://doi.org/10.5194/egusphere-2023-3029
Preprint. Discussion started: 18 January 2024

Evaluating the Wegener-Bergeron-Findeisen process in ICON in large-eddy mode with in situ observations from the CLOUDLAB project

Nadja Omanovic[1], Sylvaine Ferrachat[1], Christopher Fuchs[1], Jan Henneberger[1], Anna J. Miller[1], Kevin Ohneiser[2], Fabiola Ramelli[1], Patric Seifert[2], Robert Spirig[1], Huiying Zhang[1], and Ulrike Lohmann[1]

[1]Institute for Atmospheric and Climate Science, ETH Zürich, Zurich, Switzerland
[2]Leibniz Institute for Tropospheric Research (TROPOS), Leipzig, Germany

Correspondence: Nadja Omanovic (nadja.omanovic@env.ethz.ch) and Ulrike Lohmann (ulrike.lohmann@env.ethz.ch)

Abstract. The ice phase in clouds is essential for precipitation formation over continents. The underlying processes for ice growth are still poorly understood, leading to large uncertainties in precipitation forecasts and climate simulations. One crucial aspect is the Wegener-Bergeron-Findeisen (WBF) process, which describes the growth of ice crystals at the expense of cloud droplets leading to a partial or full glaciation of the cloud. In the CLOUDLAB project, we employ glaciogenic cloud seeding to initiate the ice phase in supercooled low-level clouds in Switzerland using uncrewed aerial vehicles with the goal to investigate the WBF process. An extensive set-up of ground-based remote sensing and balloon-borne in situ instrumentation allows us to observe the formation and subsequent growth of ice crystals in great detail. In this study, we compare the seeding signals observed in the field to those simulated using a numerical weather model in large-eddy mode (ICON-LEM). We first demonstrate the capability of the model to accurately simulate and reproduce the seeding experiments across different environmental conditions. Second, we investigate the WBF process in the model by comparing the simulated cloud droplet and ice crystal number concentration changes to in situ measurements. In the field experiments, simultaneous reductions in cloud droplet number concentrations with increased ice crystal number concentrations were observed with periods showing a full depletion of cloud droplets. The model can reproduce the observed ice crystal number concentrations most of the time, but not the observed fast reductions in cloud droplet number concentrations. Our detailed analysis shows that the WBF process appears to be less efficient in the model than in the field. In the model, exaggerated ice crystal number concentrations are required to produce comparable changes in cloud droplet number concentrations, highlighting the inefficiency of the WBF process in ICON.

1 Introduction

The ice phase is responsible for more than 70 % of precipitating clouds over continents and thus is essential for producing precipitation (Mülmenstädt et al., 2015; Heymsfield et al., 2020). The precipitation mainly originates from mixed-phase clouds, where ice crystals and cloud droplets coexist in an unstable thermodynamic equilibrium owing to subzero temperatures. In a mixed-phase cloud, three situations are possible: (i) both cloud droplets and ice crystals can grow if the ambient water vapor pressure (e) exceeds saturation with respect to liquid water ($e_{s,w}$); (ii) ice crystals grow at the expense of evaporating cloud droplets if the ambient water vapor pressure e lies between the saturation water vapor pressure with respect to ice and water ($e_{s,i} < e < e_{s,w}$); (iii) both cloud droplets and ice crystals evaporate ($e < e_{s,w}$) (Korolev, 2007). The second case is the Wegener-Bergeron-Findeisen (WBF) process, which is caused by the difference in supersaturation between the liquid and ice phase (Wegener, 1911; Bergeron, 1935; Findeisen, 1938). Whether e exceeds $e_{s,w}$ or not depends, among other factors, on the vertical velocity as a source for water vapor, and on the integrated ice crystal surface (ice crystal number concentration × mean ice crystal radius), which depletes supersaturation by consuming the available water vapor (Korolev and Mazin, 2003; Korolev, 2007). The ice crystals thereby speed up the formation of precipitation as they can rapidly grow to sizes where they sediment and induce collisions with other hydrometeors enabling further growth. Storelvmo and Tan (2015) showed the importance of the WBF process and how numerical models try to represent it within their grid scale. The parameterization of the WBF process directly impacts the representation of the liquid phase in mixed-phase clouds, which in turn impacts precipitation formation and patterns (Mülmenstädt et al., 2015; Heymsfield et al., 2020). This further influences the radiative responses of clouds (Xie et al., 2008). Currently, models can show a too-strong depletion of the liquid phase by the ice phase (Liu et al., 2011; McIlhattan et al., 2017; Huang et al., 2021) or a too-weak WBF process (Klaus et al., 2016; Kretzschmar et al., 2019) compared to observations. More studies focusing on the WBF process are therefore needed, which is the purpose of this work.

For the WBF process to take place in a cloud, ice crystals first need to form. They essentially follow two formation pathways: either via homogeneous (T < -38 °C) or heterogeneous nucleation (T > -38 °C), where the latter is essential for ice formation in mixed-phase clouds. Heterogeneous nucleation requires aerosols, so-called ice nucleating particles (INPs), to provide a surface for the ice to form on. These particles have numerous origins, with mineral dust being the most prominent natural INP, because it causes ice crystal nucleation over a wide range of temperatures (Hoose and Möhler, 2012; Murray et al., 2012; Ladino Moreno et al., 2013). The nucleation efficiency of INPs strongly decreases with increasing temperatures, where the lowest INP activity occurs close to the melting point of water. There, mainly fungal spores and bacteria are able to act as INPs, but due to their low abundance, there is generally a very low availability of INPs at temperatures close to 0 °C (Kanji et al., 2017).

This low INP availability at high temperatures can be exploited by glaciogenic cloud seeding to study the relevance of the WBF process. The general approach is to deliberately inject INPs into supercooled clouds to initiate ice formation and thus the subsequent growth of ice crystals to precipitation-sized particles (Haupt et al., 2018; Flossmann et al., 2019). The very first cloud seeding experiments date back to the 1940s and were conducted using dry ice or silver iodide (AgI) (Schaefer, 1946; Vonnegut, 1947). AgI serves as a particularly good INP with high ice activity at temperatures up to -5 °C due to its molecular lattice structure which closely resembles that of ice (DeMott, 1995; Marcolli et al., 2016). This led to worldwide programs that actively pursued increasing precipitation over land to mitigate water scarcity (e.g. Woodley et al., 2003; Griffith et al., 2009; Geerts et al., 2010; Manton and Warren, 2011; Sin'kevich et al., 2018; Yang et al., 2018; Kulkarni et al., 2019; Wang et al., 2019; Al Hosari et al., 2021; Benjamini et al., 2023). Often, wintertime orographic clouds are targeted for glaciogenic cloud seeding experiments, as the lifting of air along mountain slopes induces a high supercooled liquid water content, which serves as a water source for the ice crystals to grow (French et al., 2018; Tessendorf et al., 2019). Convective cells, which usually exhibit a larger content of supercooled water, are often too turbulent to successfully study the impact of cloud seeding with an observational setup (Flossmann et al., 2019). Such chaotic characteristics and the missing controlled reproducibility in field experiments obscure the feasibility of weather modifications (Haupt et al., 2018; Rauber et al., 2019). Only recently, the cloud seeding project SNOWIE was carried out to assess the impact of cloud seeding, from the release of seeding particles to the hydrometeor sedimentation with a focus on precipitation enhancement, and thus to study the whole microphysical process chain after initial ice formation and growth (French et al., 2018; Tessendorf et al., 2019). However, the limited observations of ice formation and growth processes active in the clouds further obscure the feasibility of glaciogenic cloud seeding (Flossmann et al., 2019).

Complementary to such field experiments, numerical models are employed to shed light on the statistical significance of cloud seeding by conducting repeated simulations. Even though some processes are missing or simplified in models (Rauber et al., 2019; Morrison et al., 2020), they offer a way to quantify the impact of cloud seeding on a broader scale. One of the very first modelling studies on cloud seeding was conducted by Meyers et al. (1995) based on the laboratory studies of AgI ice nucleation activity from DeMott (1995). They reproduced field studies from the 1980s (Deshler et al., 1990) and successfully demonstrated an increase of precipitation in their seeded case. More recently, Xue et al. (2013a, b) investigated the seeding impact on orographic clouds and showed an increase in the effectiveness of cloud seeding if the INPs are injected directly into the cloud by airborne seeding as opposed to from the ground. Other modeling studies on convective clouds found similar results (e.g., Reisin et al., 1996; Ćurić et al., 2007; Chen and Xiao, 2010). More recent studies showed the importance of higher resolutions for evaluating the impact of cloud seeding. They employed a weather model in 100 m horizontal resolution, i.e. they conducted large-eddy simulations (LES), and reproduced the environmental conditions and the dispersion of the seeding plume (Xue et al., 2016; Chu et al., 2017; Xue et al., 2022).

In this study, we evaluate the impact of cloud seeding in a numerical weather model (ICON, Zängl et al. (2015)) by utilizing seeding experiments conducted within the CLOUDLAB project. CLOUDLAB aims to improve our understanding of ice crystal formation and growth by exploiting the methodology of glaciogenic cloud seeding in dynamically stable clouds (Henneberger et al., 2023). Persistent low stratus clouds proved to be a good natural laboratory given their persistent and frequent occurrence over Switzerland during wintertime. To conduct the seeding experiments, an uncrewed aerial vehicle (UAV) is flown into the cloud to release seeding particles (AgI) upstream of the field site. The particles are then advected downstream to the field site by the wind, where the seeding-induced microphysical changes (i.e., formation and growth of ice crystals) are observed by an extensive remote sensing setup together with in situ instrumentation at high spatio-temporal resolution (Henneberger et al., 2023; Miller et al., 2023). This approach allows for repeated and laboratory-like experiments in quick succession, offering the ideal opportunity to evaluate microphysical schemes in models. By improving the parameterizations of ice growth in ICON with updated equations, CLOUDLAB aims to increase precipitation forecast skills of numerical weather prediction models by first evaluating the seeding method in a high-resolution model.

Here, we present a series of LES using ICON (Zängl et al., 2015) focusing on the WBF process within the framework of CLOUDLAB. Section 2 introduces the observational setup in CLOUDLAB, our model setup including the new seeding parameterization, as well as the methods and data used for the analysis. To evaluate the WBF process within ICON, we first validated the ability of the model to reproduce the environmental conditions, such as temperature and cloud cover (Sect. 3.1). Afterwards, we conducted several seeding simulations to show the ability of the model to reproduce the seeding signal from selected field seeding experiments including the temperature dependency of the seeding parameterization and the dilution of the seeding plume (Sect. 3.2). Based on these simulations, we analyze the efficiency of the WBF process in the model compared to in situ observations, including the examination of the impact of the seeding particle emission rate on the WBF process (Sect. 3.3). We summarize our findings regarding the model performance with respect to simulating seeding experiments and ice crystal growth in Sect. 4.

2 Data and methods

2.1 CLOUDLAB: Observational setup

The CLOUDLAB project aims to improve the understanding of ice formation and growth through glaciogenic cloud seeding and entails three field campaigns: (1) January 2022 - March 2022, (2) December 2022 - February 2023, and (3) December 2023 - February 2024. During the first two campaigns, 55 successful seeding experiments were conducted at various temperatures, wind conditions, and seeding particle emission rates. Henneberger et al. (2023) details the observational setup including analysis of four seeding experiments of the first two campaigns. Miller et al. (2023) showed the possible seeding patterns conducted in the field experiments. Their Fig. 7 displays how in-cloud experiments consist of several seeding legs per experiment, where the UAV is flying back and forth while the seeding flare is burning for approximately 6 min. The field experiments discussed in this study were performed with 4 legs of 400 m each. Here, we focus on five seeding experiments which were conducted on two consecutive days: Three experiments on 25 January 2023 (S25-2, S25-2.5, S25-3), which are also discussed in Henneberger et al. (2023), and two experiments on 26 January 2023 (S26-2.5a, S26-2.5b). We closely followed the seeding distances from the field site, the seeding patterns, and the seeding start time (Table 1). The seeding simulations are named by combining their experiment date and their seeding distance, e.g. the seeding experiment on 25 January 2023 at 2.5 km distance is called S25-2.5. For 26 January 2023, where both experiments are identical in their setup, we introduced an additional identifier in the form of "a" and "b", i.e. S26-2.5a and S26-2.5b.

Both January days were characterized by low stratus clouds and low temperatures, which are the targeted conditions for conducting seeding experiments in this project. Here, we only briefly discuss the relevant instrumentation, and a full description of the experimental approach and instrumentation can be found in Henneberger et al. (2023).

For model validation, we compared the model simulations to the atmospheric profiles measured by radiosondes (Sparv S1H3, Windsond) and to the radar reflectivity observed by a vertically pointing cloud radar (FMCW-94-DP, Radiometer Physics GmbH) (Sect. 3.1). The seeding simulations (Sect. 3.2) are compared to elevation scans conducted by a cloud radar (Mira-35, Metek) and in situ measurements obtained with a tethered balloon system (TBS) (Sect. 3.2.2 and 3.3). The TBS is equipped with a holographic imager for microscopic objects (HOLIMO) to observe cloud characteristics, such as cloud droplet and ice crystal number concentrations and size distributions. HOLIMO measures particle diameters in the range between 6 $\mu\mathrm{m}$ and 2 mm (Ramelli et al., 2020). Given the non-spherical shape of ice crystals, a mean area equivalent radius is calculated for a

https://doi.org/10.5194/egusphere-2023-3029
Preprint. Discussion started: 18 January 2024

more direct comparison to the model data in Fig. 10. The differentiation between cloud droplets and ice crystals is based on the particle's shape for radii larger than 25 µm. Anything below that is identified as cloud droplets due to the resolution limit of HOLIMO. After applying a neural network (Touloupas et al., 2020) to classify the particles into cloud droplets and ice crystals, a manual labeling of all ice crystals was conducted to minimize misclassifications. Overall following uncertainties apply: cloud droplet number concentration (± 5 %), ice crystal number concentrations for particles larger than 100 µm in diameter (5-10 %), ice crystal number concentrations for particles smaller than 100 µm in diameter (15 %) (for further information see Beck (2017) and Ramelli et al. (2021)). The HOLIMO data were analyzed with a 5 Hz frequency during the seeding experiment, whereas the background cloud was analyzed with 1 Hz. The HOLIMO data were averaged over 5 data points over time, resulting in 1 s averages for the seeding signal and 5 s for the background. The time periods before and after seeding are used to observe the unperturbed background characteristics of the cloud. We further assume that the highly localized measurements by HOLIMO serve as a representative sample of the cloud characteristics inside the seeding plume and of the background due to dynamically almost stable and persistent low stratus clouds.

2.2 Model and simulation description

We employed the numerical weather prediction model ICON-2.6.5 (Zängl et al., 2015) in a one-way nested mode (Fig. 1). The outermost nest has a 1 km horizontal resolution, 80 vertical levels, a model time step of 10 s, and is based on the operational grid of the Swiss National Meteorological Service (MeteoSwiss) (Schmidli et al., 2018). The second nest with 260 m horizontal resolution and a model time step of 2.5 s is located over the Swiss plateau, centered around the field site. The final nest is of 130 m horizontal resolution with 1 s model time step and a domain size of 40 x 30 km^2 (Fig. 1). Both inner nest also have 80 vertical levels. The initial and boundary conditions for the outermost nest are based on hourly COSMO analysis data generated by MeteoSwiss, and the simulations were initialized at 00 UTC and performed for 23 hours. For each simulation, we conducted a reference (no seeding) and a seeding simulation to quantify the impact of cloud seeding. The innermost nest with the highest resolution is the focus of this analysis. All three nests employ the ecRad scheme (Hogan and Bozzo, 2018), the "3D Smagorinsky diffusion" turbulence scheme (Lilly, 1962; Smagorinsky, 1963; Dipankar et al., 2015), and the Seifert and Beheng (2006) two-moment microphysics scheme. The cloud condensation nuclei concentration was set to 1000 cm^{-3} following Schmale et al. (2018) and is uniformly distributed in the domain. The frequency of model output was set to 5 min.

Simulations S26-2.5a and S26-2.5b are identical in their setup and serve as a proof-of-concept for the seeding approach in the model. The simulations S25-2, S25-2.5, and S25-3 highlight the impact of growth time on the seeding plume. These three simulations have been conducted at a warmer temperature than S26-2.5a and S26-2.5b. We use this difference in environmental conditions to evaluate the temperature dependence of ice nucleation induced by the seeding particles. The selection of the presented seeding simulations was constrained by how accurately the model reproduced the observed environmental conditions. Unfortunately, the model overestimated the temperatures for 25 January 2023 (Henneberger et al., 2023) (Fig. 3a), while the temperatures on the 26 January 2023 were simulated adequately (Fig. 3b). For this reason, we decided to utilize the simulation of the 26 January 2023 for both seeding days (see Sect. 3.1 for detailed discussion). While the experiments on 26 January 2023 (S26-2.5a, S26-2.5b) were simulated at the same seeding height as the field experiments (Fig. 4), the experiments on 25

https://doi.org/10.5194/egusphere-2023-3029
Preprint. Discussion started: 18 January 2024

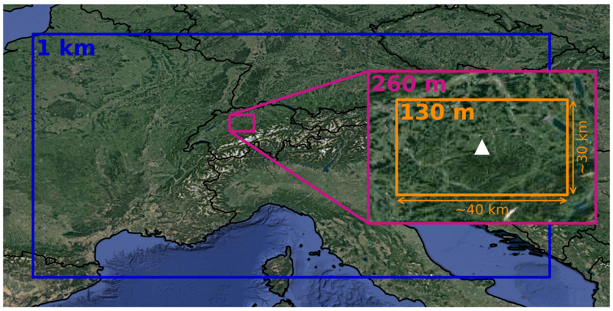

Figure 1. Nesting setup with three nests from 1 km (blue, MeteoSwiss setup), 260 m (pink) down to 130 m (orange). The CLOUDLAB field site is marked with a white triangle. The two last domains were chosen such that the field site is located in the center. Map taken from Google satellite images (©Google Maps).

Table 1. Overview of the performed seeding simulations showing the CLOUDLAB ID (ID), the simulation name given in this study (Name), the distance of the seeding location to the field site, the seeding start time (Start), the observed (Obs) and simulated (Model) temperature, wind speed and wind direction, and the growth time. Observed temperature measurements are taken from the UAV. The wind speed is calculated based on the time between seeding initiation and the first signal detected in the vertically pointing radar, and the wind direction is taken from the TBS. Based on the seeding distance and wind speed calculations, a growth time is determined assuming immediate ice nucleation of the seeding particles. Note that the last three experiments were actually performed on 25 January 2023, but due to a mismatch between model and observation temperature, still simulated on 26 January 2023 at a lower height to match the seeding temperature.

ID	Name	Distance	Date	Start	Temperature ($^{\circ}$C)		Wind speed (ms^{-1})		Wind direction ($^{\circ}$)		Growth time
		(km)		(UTC)	Obs	Model	Obs	Model	Obs	Model	(min)
SM063	S26-2.5a	2.5	26.01.	10:22	-6.4	-6.5	5.2	4.8	67	79	8.0
SM064	S26-2.5b	2.5	26.01.	10:48	-6.2	-6.5	5.8	5.4	68	80	7.1
SM059	S25-2	2.0	25.01.	10:50	-5.4	-5.6	5.5	5.5	82	77	6.1
SM058	S25-2.5	2.5	25.01.	10:28	-5.5	-5.6	5.2	4.8	81	68	8.0
SM060	S25-3	3.0	25.01.	11:15	-5.4	-5.6	5.5	4.8	89	74	9.1

January 2023 (S25-2, S25-2.5, S25-3) were simulated at a lower height such that the model temperature matches the seeding temperature from the field (-5.5 °C, Table 1).

2.3 Seeding parameterization and seeding setup

To simulate glaciogenic cloud seeding in ICON, we implemented a freezing parameterization specifically for the seeding particles (AgI) used in the field. Henneberger et al. (2023) hypothesized that the seeding particles are highly hygroscopic and postulated that these either are taken up by existing cloud droplets or undergo cloud droplet activation before freezing.

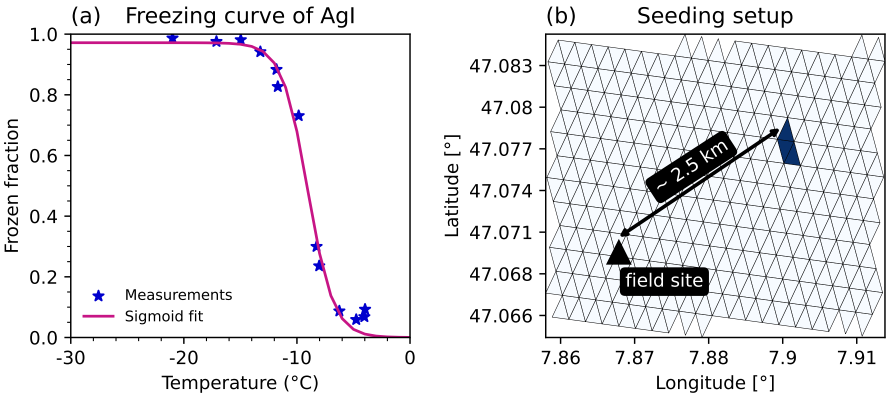

Figure 2. (a) Dependence of frozen fraction of AgI particles on temperature. Measurements (blue stars) were taken from Marcolli et al. (2016) for particle diameters of 400 nm. The pink line shows a sigmoid fit through the measurements. **(b)** Seeding setup for the S26-2.5a and S26-2.5b experiments in terms of location and distance from the field site, and with a seeding particle emission rate of $10^6\ \mathrm{m^{-3}s^{-1}}$ (marked in dark blue). The triangular grid represents the native grid of ICON.

Furthermore, their clear-sky seeding experiments showed that the seeding particles have a mean particle diameter between 100 and 400 nm. The freezing ability of AgI particles for sizes between 20 and 400 nm was measured by Marcolli et al. (2016) in a laboratory setup (their Fig. 1) showing a strong size and temperature dependence for the frozen fraction (FF). For the freezing parameterization used in the present study, we followed the 400 nm measurements, given the similar response in freezing for the larger particle sizes. We obtained the relationship

$$FF = \frac{-b}{1+\exp(-k(T-T_0))} + b, \qquad (1)$$

with the parameters $b = 0.97$, $k = 0.88$, $T_0 = 263.95\ \mathrm{K}$, and T being the temperature (K). Figure 2a shows the laboratory measurements (400 nm) of Marcolli et al. (2016), indicating an increase in frozen fraction with decreasing temperature, highlighting the strong temperature dependence of the ice activity of AgI particles. Within our model setup, we introduced the Marcolli parameterization in the two-moment microphysics scheme before the dust freezing parameterization takes place (Seifert and Beheng, 2006).

In the model, the seeding particles were introduced along a 400 m leg to mimic the seeding pattern conducted in the field experiments (see Sect. 2.2). We used the coordinates of the seeding legs to define the injection area for the seeding particles, as shown in Fig. 2b. Each conducted simulation received the same amount of seeding particle emission rate: $10^6\ \mathrm{m^{-3}s^{-1}}$ seeding particles were released in three model grid boxes for 6 min corresponding to the burning time of one seeding flare. This seeding particle emission rate is based on a series of sensitivity simulations, where we injected different concentrations of seeding particles into the model and compared the simulated ice crystal number concentrations to the observations. The seeding particle emission rate and thus seeding setup were constrained by the ice crystal number concentrations observed by HOLIMO (Sect. 3.3.1).

2.4 Detection of seeding plume

We applied a simple method to extract the seeding signal from the background. We took the difference in ice crystal number concentrations between a seeding simulation and a reference simulation (no seeding) to remove the background and isolate the seeding plume. The seeding plume was defined by a threshold ice crystal number concentration of 0.001 cm^{-3}. We used the identified seeding plume as a mask for extracting further quantities, such as cloud droplet number concentrations, temperature, and updraft changes caused by the seeding perturbation. The analysis of the seeding plume and related quantities is based on this approach to quantify the cloud seeding impact. For the comparison to in situ measurements, we considered the model output time step closest to the expected arrival of the seeding signal at the field site using the calculated growth time in Table 1.

3 Results

3.1 Model validation

To validate the model, we compared the simulated to the observed conditions on 25 and 26 January 2023. Figure 3 shows the vertical profiles of temperature and relative humidity measured by a radiosonde (solid lines) launched from the field site and predicted by the model (dashed and dotted lines). Both days were characterized by low level clouds with subzero temperatures, with 26 January showing a deeper cloud and colder temperatures. In both cases, the model did not reproduce the sharp inversions at cloud top, and for 25 January 2023, it did not simulate cold enough temperatures for the seeding particles to be effective. Therefore, we used the 26 January 2023 simulation as a surrogate for all seeding simulations (see also Sect. 2.2), as it better represents the observations on 25 January 2023 (Fig. 3a). The morning of 26 January 2023 was characterized by a strong temperature inversion at around 1.6 km above mean sea level (AMSL) limiting cloud top to that height. The model predicted a lower and weaker inversion compared to the observations with a corresponding lower cloud top. This discrepancy does not pose a problem as the observed and simulated temperatures at the seeding height (see temperature in Table 1) are in good agreement, which is the strongest constraint for our seeding simulations. Regarding the wind speed, the model performs reasonably well with slight underestimations for four of the cases (0.4 - 0.7 $\mathrm{m\,s}^{-1}$, Table 1). However, the model performs worse with regard to wind direction (± 13°, Table 1). The discrepancy in wind speed and direction does not impact the ability of the model to simulate seeding experiments.

In addition, we compared the observed and predicted cloud cover at the field site by taking the radar reflectivity of a vertically pointing radar as a proxy for cloud cover (Fig. 4). We see that the model predicts a long-lasting low cloud that reaches similar cloud top heights as observed by the radar with the seeding simulations being fully inside the cloud.

3.2 Ice response due to seeding

In the following, we discuss the seeding impact on cloud droplet and ice crystal number concentrations. We first show the evolution of the seeding plume in terms of time and location, and compare it to radar scans (Sect. 3.2.1). We then compare the

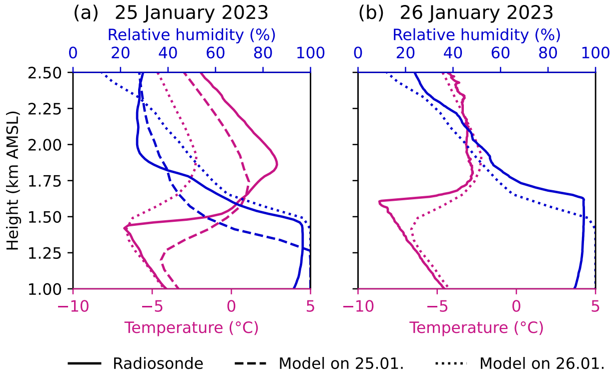

Figure 3. Comparison of radiosonde (solid lines) and model (dashed and dotted lines) profiles of the lower atmosphere for temperature (°C, pink) and relative humidity (%, blue). The simulated profiles on 25 January 2023 12:00 UTC (dashed) and 26 January 2023 10:00 UTC (dotted) are averaged over four grid points around the field site. **(a)** shows the radiosonde launch at 25 January 2023 12:08 UTC with the model output from both days, while **(b)** shows the radiosonde launch at 26 January 2023 09:29 UTC with the model output on 26 January.

observed and predicted ice crystal number concentrations for all simulations (Sect. 3.2.2). This is followed by the investigation of the WBF process in the model by utilizing the in situ measurements (Sect. 3.3). We conclude the result sections with the impact of the seeding particle emission rate on ice crystal number concentration and cloud droplet reductions (Sect. 3.3.1).

3.2.1 Evolution of the seeding plume

Here we examine the evolution of the seeding plume with respect to changes in ice crystal number concentrations in the seeding simulation S26-2.5a. The seeding plume tracks for the other simulations are in Appendix A. Figure 5 shows the response in ice crystal number concentrations at the seeding level (top view) and as a cross section along the mean wind direction at each model output time step. The first output time step (t_1) denotes the first five-min interval after the seeding start (here 10:25 UTC). We observe a strong and sudden increase in ice crystal number concentrations of up to $1\,\mathrm{cm}^{-3}$ (see Table 2) that is rapidly diluted within the first $15\,\mathrm{min}$ as the seeding plume is advected along the main wind direction. The plume also spreads out horizontally starting from several hundred meters (t_1 and t_2) to about 2 x $3\,\mathrm{km}^2$ at t_7. The seeding plume almost missed the field site (black triangle) which can be attributed to the mismatch in wind directions between the model and observations (Table 1). The seeding plume not only spreads out horizontally, but also vertically as shown in Fig. 5b, where we observe a vertical extent of up to $500\,\mathrm{m}$. Note that the ice crystal number concentrations are spread out across several hundred meters, as they are transported by turbulence and diluted strongly. We also see the sedimentation of the ice crystals as the seeding plume descends in height. Based on the applied detection method we identified the seeding plume for approximately $35\,\mathrm{min}$ before it vanished.

To evaluate the horizontal and vertical extent of the simulated seeding plume, we used elevation scans that were conducted by a scanning radar during the field experiment. The radar performed repeated elevation scans from left to right and back,

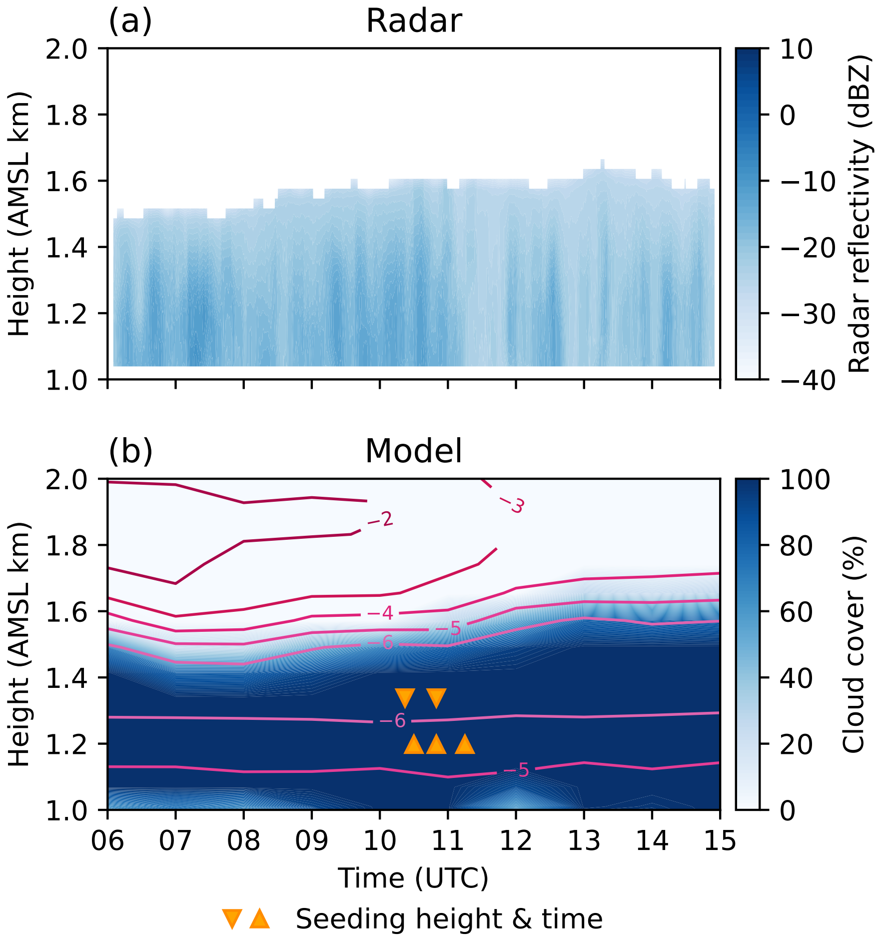

Figure 4. Temporal evolution of the measured radar reflectivity (dBZ, **(a)**) and the simulated cloud cover (%, **(b)**) at the field site as a function of height using the radar reflectivity as a proxy for cloud extent. The radar reflectivity was averaged over 5 min intervals. **(b)** in addition shows the model temperature profile (°C, pink isotherms) and the seeding simulations in terms of height and time (orange triangles). Upward facing triangles represent the simulations S25-2, S25-2.5, and S25-3, and downward facing triangles the simulation S26-2.5a and S26-2.5b.

perpendicular to the wind direction, thus allowing us to observe the horizontal and vertical extent of the seeding signal. Figure 235 6 shows the observed and simulated radar reflectivity (dBZ) at 10:30 UTC on 26 January 2023. There is a good qualitative agreement between the observed and simulated radar reflectivity with respect to the vertical extent, location, and timing of the signal.

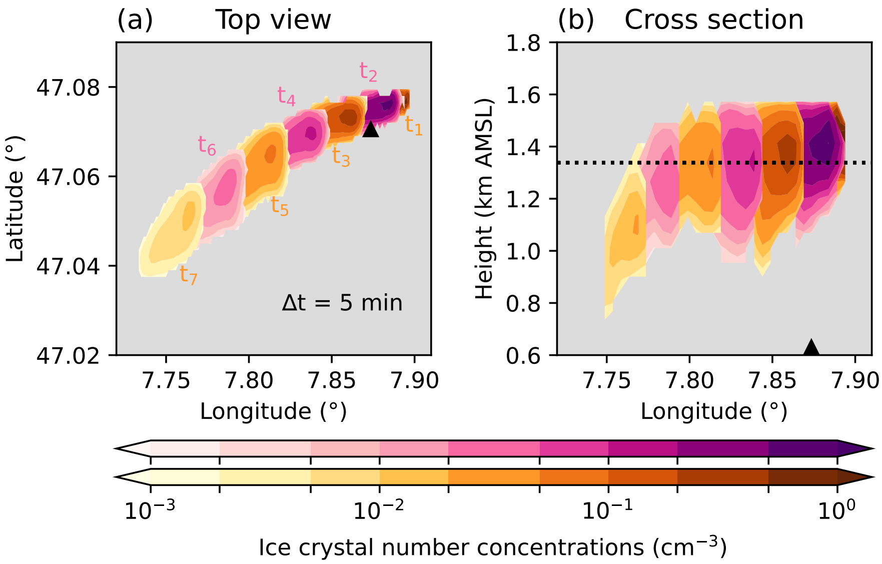

Figure 5. Simulated ice crystal number concentration changes (cm^{-3}, colormap) after seeding in simulation S26-2.5a with **(a)** showing the top view at the seeding height (dashed line in **(b)**). t_1 is the first five-min output time step after the seeding start, i.e. here 10:25 UTC. Alternating colors are used for better visibility between the output time steps. **(b)** shows the vertical cross section of the ice crystal number concentration (cm^{-3}) along the mean wind direction at the seeding height for each five-min output time step. The black triangle denotes the field site in both panels.

3.2.2 Observed vs. predicted ice crystal number concentrations

In Fig. 7, we compare the observed and predicted ice crystal number concentrations as frequency distributions for the experiments S26-2.5a and S26-2.5b. The observations were taken by the in situ instrument HOLIMO aboard the TBS over a time interval of 10 min. For both data sets, we set an ice crystal number concentration threshold of 0.001 cm^{-3}. Model predictions are based on the identified seeding plume at the time of the expected arrival of the seeding signal (see growth time in Table 1). The comparison of the measured and simulated radii is shown in Fig. 10p and discussed in Sect. 3.3.

In Fig. 7a, we see that the observed and simulated ice crystal number concentrations are in good agreement, with the model showing slightly higher concentrations (see Table 2). For experiment S26-2.5b, which has an identical setup as S26-2.5a, a similar pattern is observed (see Fig. 7b), emphasizing that the model configuration can be used to conduct seeding experiments for further investigation of the ice crystal growth inside the cloud. The seeding particle emission rate (10^6 seeding particles $\mathrm{m}^{-3}\mathrm{s}^{-1}$) used in this study is probably an upper estimate given that the environment in general is warmer (i.e., less negative temperatures below the inversion) than observed which leads to a lower activation rate of INPs than in reality. Hence, we need to introduce more seeding particles to achieve the same ice crystal number concentrations as observed.

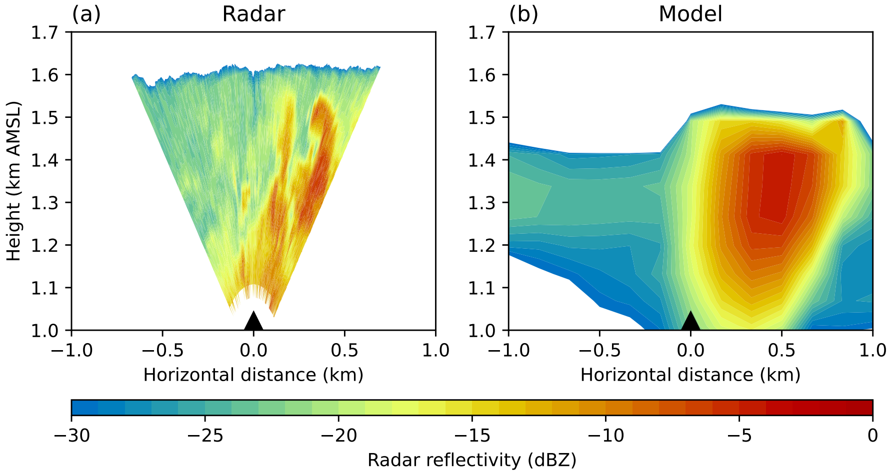

Figure 6. Comparison of the radar reflectivity measured by a scanning cloud radar (Mira-35, Metek, **(a)**) and simulated by the model (**(b)**) during seeding experiment S26-2.5a at 10:30 UTC (i.e. model output time step t_1). The field site is located in the center of the cross section (black triangle, 0.0). Both figures show a cross section of the seeding signal perpendicular to the main wind direction.

The responses in ice crystal number concentrations for the seeding simulations S25-2, S25-2.5, and S25-3, which were conducted at different seeding distances from the field site, are shown in Fig. 8. The observations indicate that with increasing seeding distance, the measured ice crystal number concentrations are reduced, indicating a dilution effect of the seeding signal. In experiment S25-2 (closest distance), we measured ice crystal number concentrations of about $2.5\,\mathrm{cm}^{-3}$, while experiment S25-3 (farthest distance), only measured concentrations of around $0.5\,\mathrm{cm}^{-3}$. The model, however, fails to reproduce the very high concentrations of S25-2, which may be due to the warmer temperature leading to a lower ice nucleation rate and due to the aerosol concentration being adapted to the simulations S26-2.5a/b. Hence, we cannot simulate the highest ice crystal number concentrations. In simulation S25-2.5, which has an identical setup as the S26-2.5a and S26-2.5b simulations except for being at $1\,^{\circ}\mathrm{C}$ warmer seeding temperatures, we can see that the ice crystal number concentrations are slightly overestimated compared to the observations (Fig. 8b). This likely results from the temperature dependency of the freezing parameterization or the exaggerated seeding particle emission rates in the model. For simulation S25-3, the model slightly underestimates the ice crystal number concentrations. This is in accordance with an efficient dilution in the model as the ice crystal number concentrations rapidly decrease with time, as shown in the seeding plume track analysis (Fig. 5, Appendix A).

3.3 Investigating the Wegener-Bergeron-Findeisen process

The in situ observations taken during the seeding experiments allow us to investigate the WBF process in greater detail. Figure 9a shows the measured cloud droplet number concentrations and Fig. 9b the ice crystal number concentrations during the seeding experiment S26-2.5a, including measurements of the undisturbed background cloud prior to and after the seeding. The analysis for the other experiments is shown in Appendix B and an overview of all experiments is given in Table 2. The

https://doi.org/10.5194/egusphere-2023-3029
Preprint. Discussion started: 18 January 2024

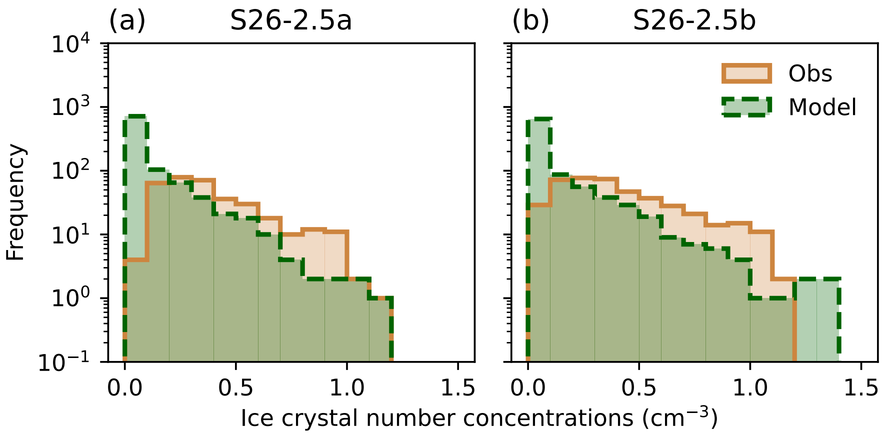

Figure 7. Frequency distributions of the observed (brown, solid) and predicted (green, dashed) ice crystal number concentrations (cm^{-3}) for experiments S26-2.5a ((**a**)) and S26-2.5b ((**b**)). The bin size is 0.1 cm^{-3}.

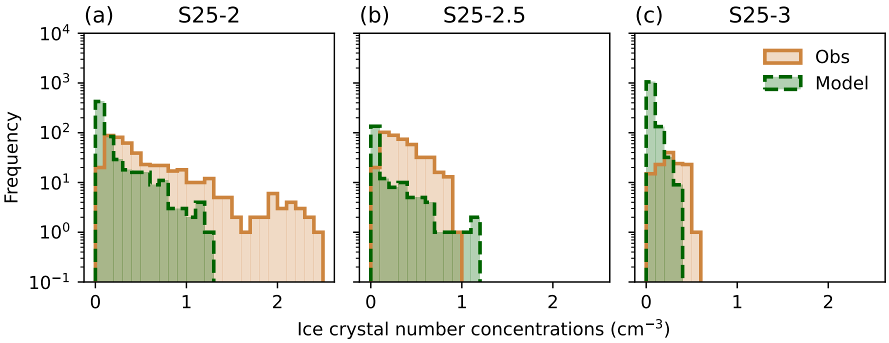

Figure 8. Frequency distributions of the observed (brown, solid) and predicted (green, dashed) ice crystal number concentrations (cm^{-3}) for experiments S25-2 ((**a**)), S25-2.5 ((**b**)), and S25-3 ((**c**)). The bin size is 0.1 cm^{-3}.

background cloud had an ice crystal number concentration of 0 cm^{-3} and a median cloud droplet number concentration of 270 320 cm^{-3} (Fig. 9). During the seeding experiment, the ice crystal number concentrations increase up to 1 cm^{-3}, whereas the cloud droplet number concentrations simultaneously decrease by up to 300 cm^{-3}.

To quantify the reduction in cloud droplets throughout the seeding experiment, we first defined the cloud droplet number concentration of the background state by calculating the median over a 20 min period of the background. Second, we considered all times in our analysis where the observed ice crystal number concentration was larger than 0.001 cm^{-3}. The time periods 275 considered in the analysis are marked by the vertical brown lines in Fig. 9a and the relative reductions in the cloud droplet number concentrations with regard to the median concentration are shown as a frequency distribution in Fig. 9c-e for different model output time steps. The observations indicate that between the seeding start and the measurements (i.e., 8 min) the liquid phase was entirely depleted during some time periods (i.e., cloud droplet reductions of 100 %), emphasizing the high efficiency of the WBF process observed in the field. Thus, the freshly nucleated ice crystals are highly efficient in consuming water vapor from the evaporating cloud droplets, leading to increased ice crystal growth and eventually isolated glaciation patches inside the cloud. These strong reductions in cloud droplets can partly originate from riming processes, where the cloud droplets immediately freeze onto the ice crystals. Only for experiments S26-2.5a/b riming was observed with HOLIMO. Here, we solely focus on the WBF process but we are aware that also the riming process can lead to additional reductions in the liquid phase. Both processes (WBF and riming) are parameterized in the model.

Next, we compare the observations to the simulated changes in the model by taking the model output time step that is closest to the time the seeding signal is expected to arrive at the field site. The changes in the model are computed from the difference between the reference and seeding simulation. Figure 9c shows both the observations and model response and we can see that the model is not able to reproduce such strong reductions in cloud droplet number concentrations, indicating that the ice crystal growth in the model is underestimated. This discrepancy may originate from the computation of the ventilation coefficient, which determines the speeding up of the diffusional growth due to turbulent motions. When looking at later model output time steps, we see that the model predicts a comparable (Fig. 9d-e) in cloud droplet number concentrations than observed. This further points to the fact that the WBF process in the model in its current form is not efficient enough.

In Table 2, we show the median and maximum ice crystal number concentrations (absolute values). For cloud droplets, we report the reduction of the median and maximum cloud droplet number concentration relative to the undisturbed background (relative values) to account for the lower median cloud droplet number concentration of approximately $100\,\mathrm{cm}^{-3}$ in the model compared to the observations (not shown). The ice crystal number concentrations are in good agreement (within $\pm\,0.3\,\mathrm{cm}^{-3}$) with observations in 4 out of 5 simulations. Only the S25-2 simulation strongly underestimates the maximum ice crystal number concentration by $1\,\mathrm{cm}^{-3}$ (see Sect. 3.2.1 and Sect. 3.2.2). Furthermore, the model was able to reproduce the maximum cloud droplet reductions for 3 out of 5 simulations. The S25-2 and S25-2.5 simulations strongly underestimate the maximum reduction showing barely any consumption of cloud droplets. However, when considering the median cloud droplet reductions (Table 2) and the full frequency distribution of cloud droplet reductions (Fig. 9 and Fig. B1) it is notable that these strong reductions only occur sporadically. This is further discussed below.

As a next step, we aim to identify when suitable conditions for the WBF process exist inside the seeding plume by applying a set of theoretical equations (Korolev and Mazin, 2003; Korolev, 2007):

$$w' < w < w^* \text{ with } w' = \frac{e_{s,i} - e_{s,w}}{e_{s,w}} N_w \overline{r}_w \chi \text{ and } w^* = \frac{e_{s,w} - e_{s,i}}{e_{s,i}} N_i \overline{r}_i \eta \qquad (2)$$

where w is the vertical velocity, w^* and w' are the computed vertical velocity thresholds, $\mathrm{e}_{s,w/i}$ are the saturation vapor pressures with respect to water and ice, respectively, $\mathrm{N}_{w/i}$ is the number concentrations for cloud droplets and ice crystals, respectively, and $\overline{r}_{w/i}$ are the mean radius for cloud droplets and ice crystals, respectively. η and χ are terms dependent on ambient temperature and pressure used to calculate the thermodynamic equilibrium. For $w > w^*$, both cloud droplets and ice crystals grow, while for $w < w'$ they shrink.

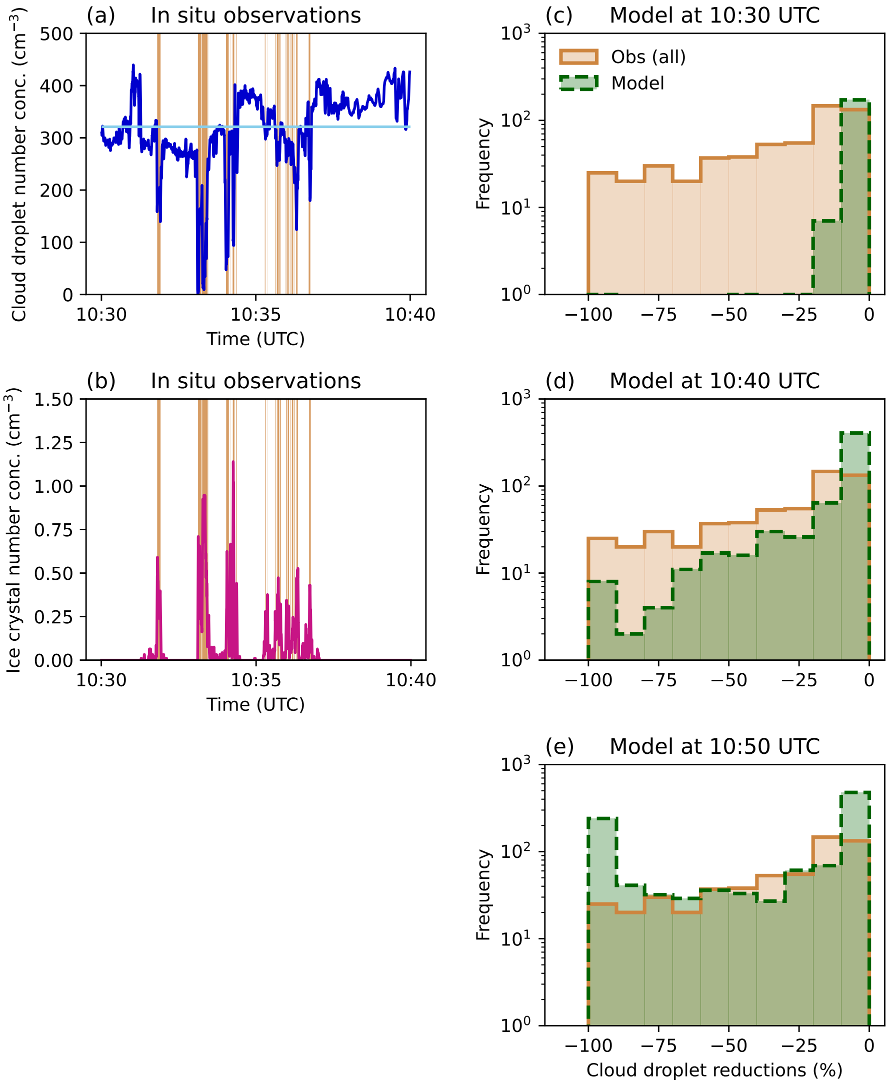

Figure 9. (a) Cloud droplet (cm^{-3}, blue) and **(b)** ice crystal number concentrations (cm^{-3}, pink) measured by HOLIMO during the seeding experiment S26-2.5a. The horizontal light blue line in **(a)** shows the median cloud droplet number concentration over a 20 min time span of background cloud prior/after the seeding. The brown shading indicates time periods where the ice crystal number concentration was above 0.001 cm^{-3}, and which were considered for the cloud droplet reduction analysis. The frequency distributions for the observed (brown, solid) and simulated (green, dashed) cloud droplet reductions are shown in **(c)-(e)** for different model output time steps. The model output time steps are 10:30 UTC, 10:40 UTC, and 10:50 UTC for the panels **(c)-(d)**, respectively. The bin size is set to 10 %.

Conditions favorable for the WBF process are therefore constrained by the vertical velocity and the integral ice crystal and cloud droplet radius. For positive vertical velocities, i.e. updrafts, the ice crystal number concentrations and mean radii define the WBF regime, while for negative vertical velocities, i.e. downdrafts, cloud droplet number concentrations and mean radii

Table 2. Median and maximum observed (Obs) and predicted (Model) ice crystal number concentrations (ICNC, $\mathrm{cm^{-3}}$) and cloud droplet reductions (CDR, %) for all five experiments. For the observations we considered the entire measurement period during the seeding experiment. For the model we considered the output time step that is closest to the time of the expected seeding signal at the field site, i.e. based on the calculated growth time in Table 1.

	ICNC ($\mathrm{cm^{-3}}$)				CDR (%)			
	Median		Maximum		Median		Maximum	
Name	Obs	Model	Obs	Model	Obs	Model	Obs	Model
S26-2.5a	0.2	0.02	1.0	1.2	-20	-0.5	-100	-90
S26-2.5b	0.2	0.02	1.2	1.3	-20	-0.6	-100	-100
S25-2	0.25	0.25	2.4	1.25	-35	-0.03	-100	-10
S25-2.5	0.15	0.03	0.9	1.2	-30	-0.002	-100	-1
S25-3	0.08	0.01	0.5	0.4	-40	-0.1	-90	-100

define the WBF regime. Hence, for $w < w^*$ the ice phase acts as a sink for the supersaturation generated by the updrafts. For $w > w'$ the liquid phase is constraining the WBF process as the downdrafts reduce the supersaturation. As long as cloud droplets are present, the serve as a source for the ice crystals to grow. We call these two conditions updraft WBF ($\mathrm{WBF}_{\uparrow}$) and downdraft WBF ($\mathrm{WBF}_{\downarrow}$). To quantify the occurrence of the WBF process, we determined for each model grid box inside the seeding plume which of these two regimes prevails (Fig. 10a-g). For most of the shown timesteps, roughly 50 % or more of the plume grid boxes are within the WBF regime. About 40 % of the time both cloud droplets and ice crystals can grow inside the plume ($w > w^*$). The simultaneous evaporation and evaporation ($w < w'$) of the hydrometeors occurs least often (10 % of the time) within the seeding plume. During WBF conditions the $\mathrm{WBF}_{\downarrow}$ is dominant, which is further supported by the vertical velocities in Fig. 10h-n, which indicate the presence of downdrafts inside the seeding plume. Based on the prognostic mass and number mixing ratio for the ice and cloud droplet phase, we calculated the ice crystal and cloud droplet radii assuming a spherical shape for all particles (Fig. 10o-ab). We can see that the mean ice crystal radius increases over time, while the mean cloud droplet radius slightly decreases, indicating that in fact the WBF process takes place. Additionally, we show the mean radius for ice crystals and cloud droplets measured by HOLIMO (see Sect. 2.1) during the seeding event (see t_2). While the the cloud droplet radius distributions match well (Fig. 10w), the model underestimates the mean ice crystal radius by almost 30 $\mu\mathrm{m}$ (Fig. 10p). Also, the observations show a broader range of ice crystal radii than was simulated. This clearly indicates that the WBF process in the model is too slow to reproduce the observed growth rates in the field and/or the turbulent motions are too weak. Finally, we diagnosed the rate of water vapor deposition onto the ice crystals during the model simulation (Fig. 10ac). Initially, we simulated the largest vapor deposition growth rates (up to $1.5 \times 10^{-4}\mathrm{gm^{-3}s^{-1}}$) with ice crystals growing the fastest, which can also be seen in the evolution of the ice crystal radius over time (Fig. 10o-ab). At later model output time steps, the rate decreases to almost $0\,\mathrm{gm^{-3}s^{-1}}$, when ice crystal no longer grow due to vapor deposition.

https://doi.org/10.5194/egusphere-2023-3029
Preprint. Discussion started: 18 January 2024

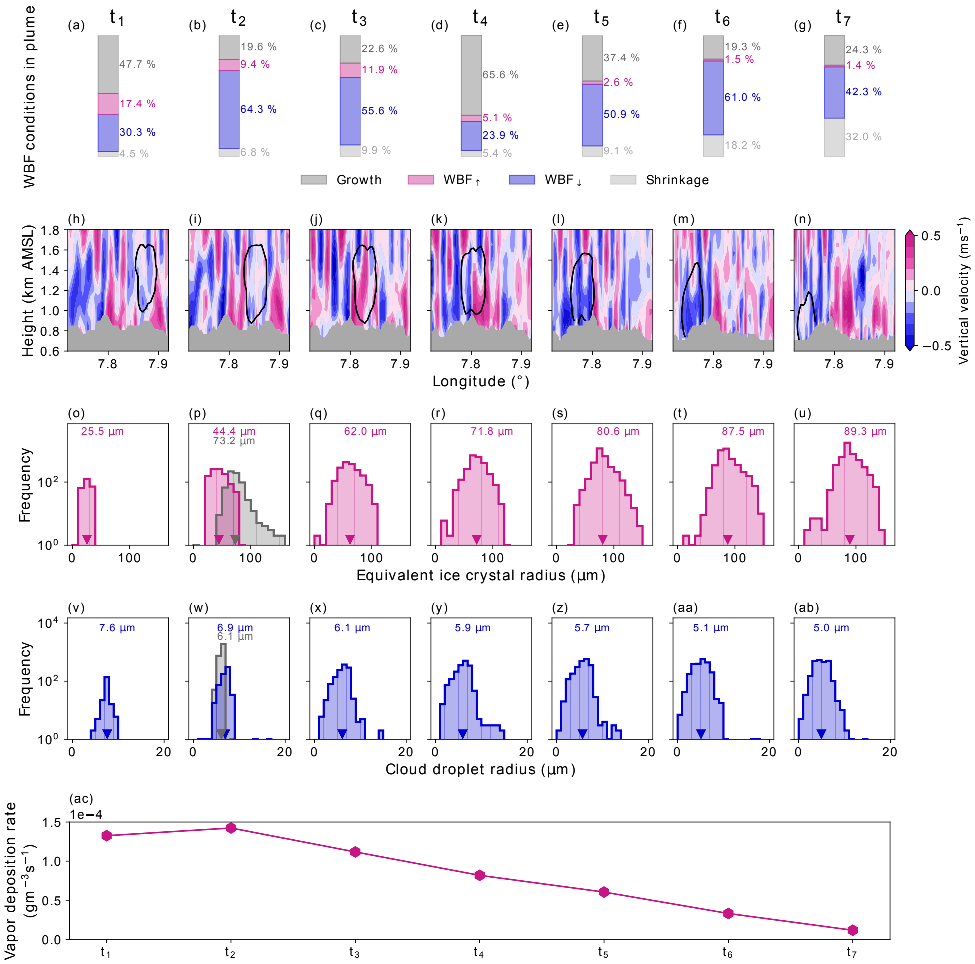

Figure 10. First row (**(a)**-**(g)**): Percentages of WBF and non-WBF conditions inside the seeding plume for experiment S26-2.5a for different model output time steps (t_1 - t_7). Conditions were determined based on Korolev and Mazin (2003) and Korolev (2007) and differentiated between "Growth" (dark grey, both cloud droplets and ice crystal grow), "WBF$_\uparrow$" (pink, WBF defined by updrafts), "WBF$_\downarrow$" (blue, WBF defined by downdrafts), and "Shrinkage" (light grey, cloud droplets evaporate and ice crystals sublimate). Second row (**(h)**-**(n)**): Cross sections of vertical velocity along the mean wind direction over time. The black contours indicate the location of the seeding plume and the grey shading denotes the topography. Third row (**(o)**-**(u)**): Frequency distribution of equivalent ice crystal radius (µm, pink) over time and mean equivalent radius (downward facing triangle, pink numerical value). Panel **(p)**, in addition, shows the mean equivalent ice crystal radius distribution (grey) measured by HOLIMO for the time period in Fig. 9b. Fourth row (**(v)**-**(ab)**): As in the third row but for cloud droplet radius (µm). Panel **(w)** depicts also the measured cloud droplet radius distribution (grey) measred by HOLIMO for the time period in Fig. 9b. Last row (**(ac)**): Simulated rate of water vapor deposition onto ice particles ($gm^{-3}s^{-1}$) over time. t_2, t_4, and t_6 correspond to the model responses shown in Fig. 9c-e.

https://doi.org/10.5194/egusphere-2023-3029
Preprint. Discussion started: 18 January 2024

3.3.1 Sensitivity analysis of seeding particle emission rate

Here we perform a sensitivity analysis to investigate the effect of the seeding particle concentration on the ice crystal number concentrations and cloud droplet reductions (Fig. 11). With $10^6\,\mathrm{m}^{-3}\mathrm{s}^{-1}$ seeding particles, the model predicts the observed ice crystal number concentrations, however, it fails to match the observed reductions in cloud droplets (Sect. 3.3, Fig. 11a). When increasing the seeding particle emission rate by a factor of three, we see that the model overestimates the ice crystal number concentrations while still underestimating the cloud droplet reductions (Fig. 11b). Only when we introduce 10 times more seeding particles than in the default configuration, the model reaches the observed cloud droplet reductions but yields much higher ice crystal number concentrations (Fig. 11c). This further supports the hypothesis that the model does not represent ice crystal growth rates accurately. Only if a high number of ice crystals is present, the observed cloud droplet reductions can be reproduced. This sensitivity analysis also shows that a seeding particle emission rate of $10^6\,\mathrm{m}^{-3}\mathrm{s}^{-1}$ is a good approximation to conduct seeding experiments in the model to match our experimental observations in the field. We also tested lower seeding particle concentrations, but then the ice crystal number concentrations were underestimated (not shown). The default setup may still be an overestimation in ice crystal number concentration due to the warmer temperatures below the inversion in the model (see Fig. 3), which leads to lower ice nucleation rates of the seeding particles given the stron temperature dependence of ice nucleation. Hence, if the model were colder, we would see a higher ice crystal number concentration. We are aware of this limitation but decided to constrain our seeding setup by the observed ice crystal number concentrations instead of the seeding particle emission rate, as the latter cannot be precisely estimated.

4 Conclusions

This study presented LES in the scope of the CLOUDLAB project aimed at reproducing the field seeding experiments and constraining the WBF process inside the model. For that, a nested LES was set up to conduct seeding simulations with the numerical weather model ICON, which includes an implementation of a new seeding parameterization for freezing of AgI particles. Five seeding experiments from two days were simulated using a single-day simulation as a surrogate, because the model failed to reproduce low enough temperatures in the boundary layer. The experiments differed in seeding temperature and distance, allowing us to investigate the temperature sensitivity of the seeding parameterization and the effect of different seeding distances from the field site on ice crystal growth and dilution.

We first showed that ICON is able to reproduce long-lasting low-level clouds but with a weaker temperature inversion. The observed seeding temperature was nevertheless eventually reached, enabling us to conduct seeding simulations. The first two simulations were conducted at a seeding temperature of -6.5 °C (S26-2.5a, S26-2.5b) and are in good agreement with observed ice crystal number concentrations obtained from the in situ device HOLIMO. In addition, the simulated extent of the seeding plume agrees qualitatively with the observations from radar scans. The measurements for the three experiments at warmer temperatures (-5.5 °C) with varying distances from the field site (2, 2.5, and 3 km) show a strong dilution effect with maximum ice crystal number concentrations up to $2.5\,\mathrm{cm}^{-3}$ for the shortest seeding distance down to $0.5\,\mathrm{cm}^{-3}$ for the furthest seeding distance. The model strongly underpredicts the ice crystal number concentrations for one of the simulations

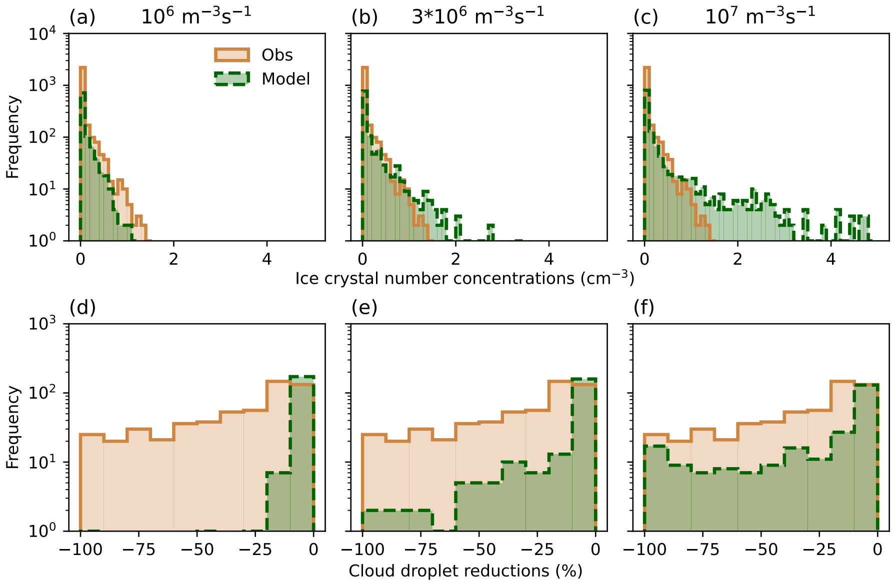

Figure 11. Upper row: Ice crystal number concentrations (cm^{-3}) of experiment S26-2.5a observed (brown, solid) by HOLIMO and simulated (green, dashed) with $10^6\ \mathrm{m}^{-3}\mathrm{s}^{-1}$ seeding particles (default seeding particle emission rate, **(a)**), $3{*}10^6\ \mathrm{m}^{-3}\mathrm{s}^{-1}$ seeding particles (**(b)**), and $10^7\ \mathrm{m}^{-3}\mathrm{s}^{-1}$ seeding particles (**(c)**). The bin size is $0.1\ \mathrm{cm}^{-3}$. Lower row: Relative changes in cloud droplet number concentrations (%) observed (brown, solid) and simulated (green. dashed) for the corresponding seeding particle concentrations. The bin size is 10 %. Note that for all panels, the observations are identical. For the model response, the difference between a seeding and a reference simulation was taken at 10:30 UTC (as in Fig. 9c).

which may originate from the fact that we chose the aerosol concentration in such a way that it agrees well with the simulations S26-2.5a/b, both of which occur at colder temperatures.

In the second part, we investigated the WBF process at high spatio-temporal resolution. The in situ measurements showed that the high ice crystal number concentrations were accompanied by reductions in cloud droplet number concentrations confirming that the WBF process took place. During the seeding experiments, we observed fully glaciated patches, i.e. where zero cloud droplet number concentrations with high ice crystal number concentrations were measured. By analyzing the relative cloud droplet reductions within the seeding plume with regard to the undisturbed background, we computed frequency distributions of observed reductions in cloud droplets. This was compared to the simulated cloud droplet number concentrations by taking the difference between a seeding simulation and a reference simulation without seeding. We showed that the model could not reproduce the observed strong reductions in cloud droplet number concentrations, supporting the hypothesis that the WBF process is too slow in the model or that tubrulent motions, which could locally enhance growth rates, are too weak. Only at later model output time steps, comparable cloud droplet reductions were achieved. By calculating the proportion of favorable conditions for the WBF process to take place inside the seeding plume and identifying the changes in cloud droplet and ice crystal radii, we showed that the WBF process takes place in the model but at a slower rate than observed in the field. We also tested the effect of increased seeding particle emission rate on ice crystal and cloud droplet changes. Tripling the seeding particle emission rate led to a slight overestimation in ice crystal number concentrations, while the reduction in cloud droplets still could not be reproduced. Only by introducing 10 times more seeding particles, we reached comparable cloud droplet reductions as in the observations. However, in this case, the ice crystal number concentrations were largely overestimated. This further supports the hypothesis that the WBF process in the model is too slow or its turbulent enhancement too weak, which in turn has implications on the efficiency of precipitation formation.

Further work will build upon these findings by perturbing the parameterization for ice crystal growth through vapor deposition via the ventilation coefficient to account for turbulent motions and by quantifying the impact of turbulence on ice crystal growth. With the final field campaign, we expect to extend our current experimental data set to have more variation in environmental conditions to further constrain ice formation and growth. This study shows the high potential of the gathered CLOUDLAB data in conjunction with a modeling approach to better understand ice crystal growth.

Code and data availability. Data and scripts available at XX. Note from authors: Data and scripts will be uploaded into a repository upon acceptance, and are available upon request until then.

https://doi.org/10.5194/egusphere-2023-3029
Preprint. Discussion started: 18 January 2024

Appendix A: Seeding plume tracking

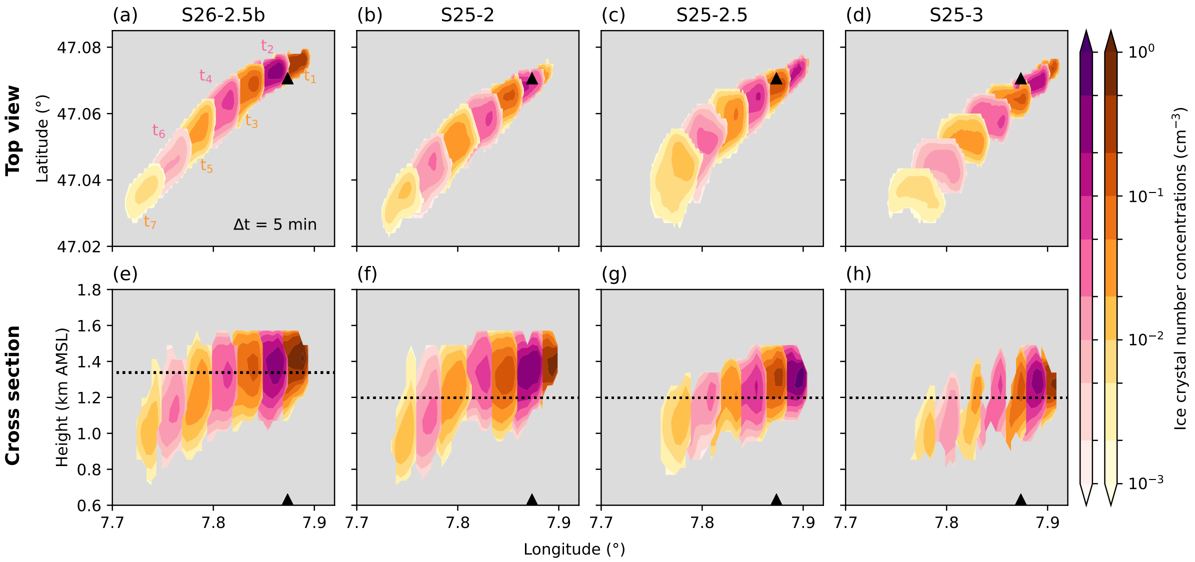

Figure A1. Simulated ice crystal number concentration changes (cm^{-3}, colormap) after seeding in simulations S26-2.5b (first column), S25-2 (second column), S25-2.5 (third column) and S25-3 (fourth column) with **(a), (b), (c), (d)** showing the top view at seeding height (dashed line in **(e), (f), (g), (h)**): t_1 is the first five-min output time step after seeding start. Alternating colors are used for better visibility between the output time steps. **(e), (f), (g), (h)** show the vertical cross sections in ice crystal number concentrations (cm^{-3}) along the mean wind direction at the seeding height for each output time step. The black triangle denotes the field site in all panels.

Appendix B: WBF investigation

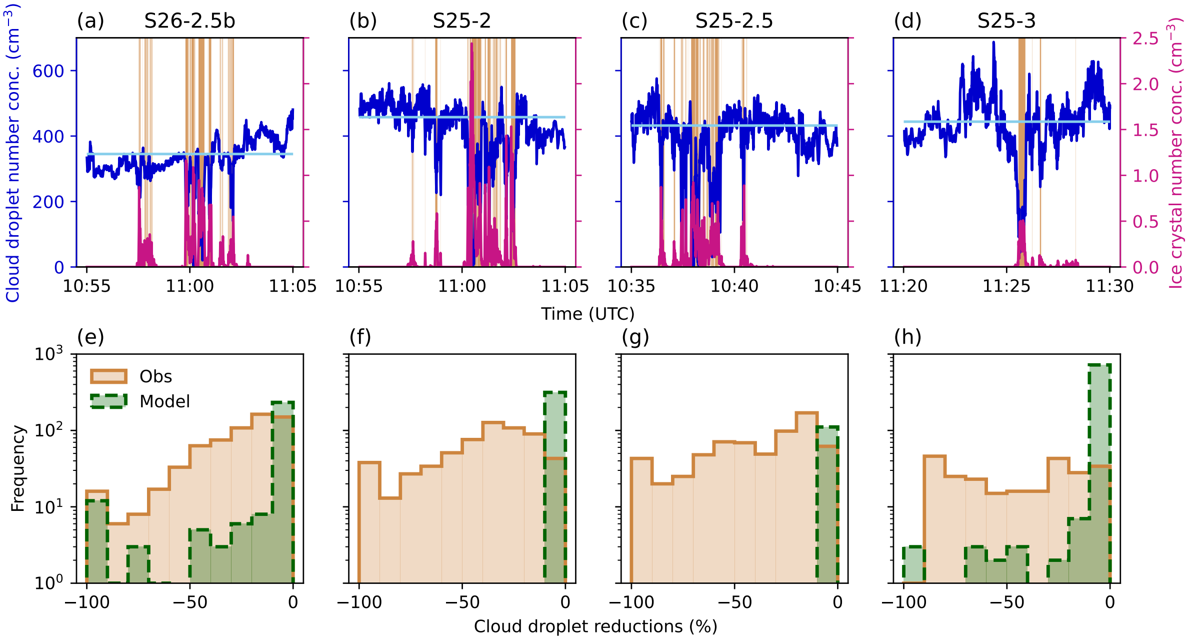

Figure B1. Upper row: Cloud droplet (cm^{-3}, blue) and ice crystal (cm^{-3}, pink) concentrations measured by HOLIMO during the four experiments S26-2.5b (**(a)**), S25-2 (**(b)**), S25-2.5 (**(c)**), and S25-3 (**(d)**). Horizontal light blue lines show for each experiment the median cloud droplet number concentration over 20 min time span of the background cloud prior/after seeding. The brown shading indicates time periods where the ice crystal number concentration was above 0.001 cm^{-3} and which were considered for the cloud droplet reduction analysis. The frequency distribution for the observed (brown, solid) and simulated (green, dashed) cloud droplet reductions are shown in the lower row (**(e)**-**(h)**). The bin size is set to 10 %.

Author contributions. UL, JH, FR conceived of the idea of CLOUDLAB and obtained funding. NO, CF, JH, AJM, FR, RS, HZ designed and conducted the in-cloud seeding experiment presented here, with conceptual input from UL. CF conducted the entire analysis of HOLIMO data. KO, PS provided the vertically pointing radar used for model verification. NO, SF implemented the AgI freezing parameterization in ICON. NO set up the model nesting, performed all simulations and subsequent analysis with the here presented figures. NO, SF, UL contributed to the interpretation of the results. NO wrote the manuscript. All authors contributed to the editing and review of the manuscript.

Competing interests. The authors declare that they have no conflict of interest.

Acknowledgements. The CLOUDLAB project has received funding from the European Research Council (ERC) 411 under the European Union's Horizon 2020 research and innovation program (grant agreement 412 No. 101021272 CLOUDLAB). This work was supported by a grant from the Swiss National Supercomputing Centre (CSCS) under project ID s1144. We further want to thank Stephanie Westerhuis and Brigitta Goger for their support during the model setup by providing model grids and scripts to generate the initial and boundary conditions and their continuous helpful input regarding model validation.

References

Al Hosari, T., Al Mandous, A., Wehbe, Y., Shalaby, A., Al Shamsi, N., Al Naqbi, H., Al Yazeedi, O., Al Mazroui, A., and Farrah, S.: The UAE Cloud Seeding Program: A Statistical and Physical Evaluation, Atmosphere, 12, 1013, https://doi.org/10.3390/atmos12081013, 2021.

Beck, A.: Observing the Microstructure of Orographic Clouds with HoloGondel, Doctoral thesis, ETH Zurich, Zurich, https://doi.org/10.3929/ethz-b-000250847, 2017.

Benjamini, Y., Givati, A., Khain, P., Levi, Y., Rosenfeld, D., Shamir, U., Siegel, A., Zipori, A., Ziv, B., and Steinberg, D. M.: The Israel 4 Cloud Seeding Experiment: Primary Results, Journal of Applied Meteorology and Climatology, 62, 317–327, https://doi.org/10.1175/JAMC-D-22-0077.1, 2023.

Bergeron, T.: On the physics of clouds and precipitation, Proc. 5th Assembly UGGI, Lisbon, Portugal, 1935, p. 156–180, 1935.

Chen, B. and Xiao, H.: Silver iodide seeding impact on the microphysics and dynamics of convective clouds in the high plains, Atmospheric Research, 96, 186–207, https://doi.org/10.1016/j.atmosres.2009.04.001, 2010.

Chu, X., Geerts, B., Xue, L., and Pokharel, B.: A Case Study of Cloud Radar Observations and Large-Eddy Simulations of a Shallow Stratiform Orographic Cloud, and the Impact of Glaciogenic Seeding, Journal of Applied Meteorology and Climatology, 56, 1285 – 1304, https://doi.org/10.1175/JAMC-D-16-0364.1, 2017.

DeMott, P.: Quantitative descriptions of ice formation mechanisms of silver iodide-type aerosols, Atmospheric Research, 38, 63–99, https://doi.org/https://doi.org/10.1016/0169-8095(94)00088-U, 1995.

Deshler, T., Reynolds, D. W., and Huggins, A. W.: Physical Response of Winter Orographic Clouds over the Sierra Nevada to Airborne Seeding Using Dry Ice or Silver Iodide, Journal of Applied Meteorology and Climatology, 29, 288–330, https://doi.org/10.1175/1520-0450(1990)029<0288:PROWOC>2.0.CO;2, 1990.

Dipankar, A., Stevens, B., Heinze, R., Moseley, C., Zängl, G., Giorgetta, M., and Brdar, S.: Large Eddy Simulation Using the General Circulation Model ICON, Journal of Advances in Modeling Earth Systems, 7, 963–986, https://doi.org/10.1002/2015MS000431, 2015.

Findeisen, W.: Kolloid-meteorologische Vorgänge bei der Niederschlagsbildung, Meteorologische Zeitschrift, 55, 121–133, 1938.

Flossmann, A. I., Manton, M., Abshaev, A., Bruintjes, R., Murakami, M., Prabhakaran, T., and Yao, Z.: Review of Advances in Precipitation Enhancement Research, Bulletin of the American Meteorological Society, 100, 1465–1480, https://doi.org/10.1175/BAMS-D-18-0160.1, 2019.

French, J. R., Friedrich, K., Tessendorf, S. A., Rauber, R. M., Geerts, B., Rasmussen, R. M., Xue, L., Kunkel, M. L., and Blestrud, D. R.: Precipitation Formation from Orographic Cloud Seeding, Proceedings of the National Academy of Sciences, 115, 1168–1173, https://doi.org/10.1073/pnas.1716995115, 2018.

Geerts, B., Miao, Q., Yang, Y., Rasmussen, R., and Breed, D.: An Airborne Profiling Radar Study of the Impact of Glaciogenic Cloud Seeding on Snowfall from Winter Orographic Clouds, Journal of the Atmospheric Sciences, 67, 3286–3302, https://doi.org/10.1175/2010JAS3496.1, 2010.

Griffith, D. A., Solak, M. E., and Yorty, D. P.: 30+ Winter Seasons Of Operational Cloud Seeding In Utah, The Journal of Weather Modification, 41, 23–37, https://doi.org/10.54782/jwm.v41i1.175, 2009.

Haupt, S. E., Rauber, R. M., Carmichael, B., Knievel, J. C., and Cogan, J. L.: 100 Years of Progress in Applied Meteorology. Part I: Basic Applications, Meteorological Monographs, 59, 22.1–22.33, https://doi.org/10.1175/AMSMONOGRAPHS-D-18-0004.1, 2018.

Henneberger, J., Ramelli, F., Spirig, R., Omanovic, N., Miller, A. J., Fuchs, C., Zhang, H., Bühl, J., Hervo, M., Kanji, Z. A., Ohneiser, K., Radenz, M., Rösch, M., Seifert, P., and Lohmann, U.: Seeding of Supercooled Low Stratus Clouds with a UAV to Study

https://doi.org/10.5194/egusphere-2023-3029
Preprint. Discussion started: 18 January 2024

Microphysical Ice Processes - An Introduction to the CLOUDLAB Project, Bulletin of the American Meteorological Society, -1, https://doi.org/10.1175/BAMS-D-22-0178.1, 2023.

Heymsfield, A. J., Schmitt, C., Chen, C.-C.-J., Bansemer, A., Gettelman, A., Field, P. R., and Liu, C.: Contributions of the Liquid and Ice Phases to Global Surface Precipitation: Observations and Global Climate Modeling, Journal of the Atmospheric Sciences, 77, 2629 – 2648, https://doi.org/10.1175/JAS-D-19-0352.1, 2020.

Hogan, R. J. and Bozzo, A.: A Flexible and Efficient Radiation Scheme for the ECMWF Model, Journal of Advances in Modeling Earth Systems, 10, 1990–2008, https://doi.org/https://doi.org/10.1029/2018MS001364, 2018.

Hoose, C. and Möhler, O.: Heterogeneous Ice Nucleation on Atmospheric Aerosols: A Review of Results from Laboratory Experiments, Atmospheric Chemistry and Physics, 12, 9817–9854, https://doi.org/10.5194/acp-12-9817-2012, 2012.

Huang, Y., Dong, X., Kay, J. E., Xi, B., and McIlhattan, E. A.: The Climate Response to Increased Cloud Liquid Water over the Arctic in CESM1: A Sensitivity Study of Wegener–Bergeron–Findeisen Process, Climate Dynamics, 56, 3373–3394, https://doi.org/10.1007/s00382-021-05648-5, 2021.

Kanji, Z. A., Ladino, L. A., Wex, H., Boose, Y., Burkert-Kohn, M., Cziczo, D. J., and Krämer, M.: Overview of Ice Nucleating Particles, Meteorological Monographs, 58, 1.1 – 1.33, https://doi.org/10.1175/AMSMONOGRAPHS-D-16-0006.1, 2017.

Klaus, D., Dethloff, K., Dorn, W., Rinke, A., and Wu, D. L.: New Insight of Arctic Cloud Parameterization from Regional Climate Model Simulations, Satellite-Based, and Drifting Station Data, Geophysical Research Letters, 43, 5450–5459, https://doi.org/10.1002/2015GL067530, 2016.

Korolev, A.: Limitations of the Wegener–Bergeron–Findeisen Mechanism in the Evolution of Mixed-Phase Clouds, Journal of the Atmospheric Sciences, 64, 3372–3375, https://doi.org/10.1175/JAS4035.1, 2007.

Korolev, A. V. and Mazin, I. P.: Supersaturation of Water Vapor in Clouds, Journal of the Atmospheric Sciences, 60, 2957–2974, https://doi.org/10.1175/1520-0469(2003)060<2957:SOWVIC>2.0.CO;2, 2003.

Kretzschmar, J., Salzmann, M., Mülmenstädt, J., and Quaas, J.: Arctic Clouds in ECHAM6 and Their Sensitivity to Cloud Microphysics and Surface Fluxes, Atmospheric Chemistry and Physics, 19, 10 571–10 589, https://doi.org/10.5194/acp-19-10571-2019, 2019.

Kulkarni, J. R., Morwal, S. B., and Deshpande, N. R.: Rainfall Enhancement in Karnataka State Cloud Seeding Program “Varshadhare” 2017, Atmospheric Research, 219, 65–76, https://doi.org/10.1016/j.atmosres.2018.12.020, 2019.

Ladino Moreno, L. A., Stetzer, O., and Lohmann, U.: Contact Freezing: A Review of Experimental Studies, Atmospheric Chemistry and Physics, 13, 9745–9769, https://doi.org/10.5194/acp-13-9745-2013, 2013.

Lilly, D. K.: On the numerical simulation of buoyant convection, Tellus, 14, 148–172, https://doi.org/https://doi.org/10.1111/j.2153-3490.1962.tb00128.x, 1962.

Liu, X., Xie, S., Boyle, J., Klein, S. A., Shi, X., Wang, Z., Lin, W., Ghan, S. J., Earle, M., Liu, P. S. K., and Zelenyuk, A.: Testing Cloud Microphysics Parameterizations in NCAR CAM5 with ISDAC and M-PACE Observations, Journal of Geophysical Research: Atmospheres, 116, https://doi.org/10.1029/2011JD015889, 2011.

Manton, M. J. and Warren, L.: A Confirmatory Snowfall Enhancement Project in the Snowy Mountains of Australia. Part II: Primary and Associated Analyses, Journal of Applied Meteorology and Climatology, 50, 1448–1458, https://doi.org/10.1175/2011JAMC2660.1, 2011.

Marcolli, C., Nagare, B., Welti, A., and Lohmann, U.: Ice Nucleation Efficiency of AgI: Review and New Insights, Atmospheric Chemistry and Physics, 16, 8915–8937, https://doi.org/10.5194/acp-16-8915-2016, 2016.

McIlhattan, E. A., L’Ecuyer, T. S., and Miller, N. B.: Observational Evidence Linking Arctic Supercooled Liquid Cloud Biases in CESM to Snowfall Processes, Journal of Climate, 30, 4477–4495, https://doi.org/10.1175/JCLI-D-16-0666.1, 2017.

Meyers, M. P., Demott, P. J., and Cotton, W. R.: A Comparison of Seeded and Nonseeded Orographic Cloud Simulations with an Explicit Cloud Model, Journal of Applied Meteorology and Climatology, 34, 834 – 846, https://doi.org/10.1175/1520-0450(1995)034<0834:ACOSAN>2.0.CO;2, 1995.

Miller, A. J., Ramelli, F., Fuchs, C., Omanovic, N., Spirig, R., Zhang, H., Lohmann, U., Kanji, Z. A., and Henneberger, J.: Two new multirotor UAVs for glaciogenic cloud seeding and aerosol measurements within the CLOUDLAB project, Atmospheric Measurement Techniques Discussions, 2023, 1–30, https://doi.org/10.5194/amt-2023-157, 2023.

Morrison, H., van Lier-Walqui, M., Fridlind, A. M., Grabowski, W. W., Harrington, J. Y., Hoose, C., Korolev, A., Kumjian, M. R., Milbrandt, J. A., Pawlowska, H., Posselt, D. J., Prat, O. P., Reimel, K. J., Shima, S.-I., van Diedenhoven, B., and Xue, L.: Confronting the Challenge of Modeling Cloud and Precipitation Microphysics, Journal of Advances in Modeling Earth Systems, 12, e2019MS001 689, https://doi.org/10.1029/2019MS001689, 2020.

Mülmenstädt, J., Sourdeval, O., Delanoë, J., and Quaas, J.: Frequency of Occurrence of Rain from Liquid-, Mixed-, and Ice-Phase Clouds Derived from A-Train Satellite Retrievals, Geophysical Research Letters, 42, 6502–6509, https://doi.org/10.1002/2015GL064604, 2015.

Murray, B. J., O'Sullivan, D., Atkinson, J. D., and Webb, M. E.: Ice Nucleation by Particles Immersed in Supercooled Cloud Droplets, Chemical Society Reviews, 41, 6519–6554, https://doi.org/10.1039/C2CS35200A, 2012.

Ramelli, F., Beck, A., Henneberger, J., and Lohmann, U.: Using a holographic imager on a tethered balloon system for microphysical observations of boundary layer clouds, Atmospheric Measurement Techniques, 13, 925–939, https://doi.org/10.5194/amt-13-925-2020, 2020.

Ramelli, F., Henneberger, J., David, R. O., Bühl, J., Radenz, M., Seifert, P., Wieder, J., Lauber, A., Pasquier, J. T., Engelmann, R., Mignani, C., Hervo, M., and Lohmann, U.: Microphysical investigation of the seeder and feeder region of an Alpine mixed-phase cloud, Atmospheric Chemistry and Physics, 21, 6681–6706, https://doi.org/10.5194/acp-21-6681-2021, 2021.

Rauber, R. M., Geerts, B., Xue, L., French, J., Friedrich, K., Rasmussen, R. M., Tessendorf, S. A., Blestrud, D. R., Kunkel, M. L., and Parkinson, S.: Wintertime Orographic Cloud Seeding—A Review, Journal of Applied Meteorology and Climatology, 58, 2117–2140, https://doi.org/10.1175/JAMC-D-18-0341.1, 2019.

Reisin, T., Levin, Z., and Tzivion, S.: Rain Production in Convective Clouds As Simulated in an Axisymmetric Model with Detailed Microphysics. Part I: Description of the Model, Journal of the Atmospheric Sciences, 53, 497–519, https://doi.org/10.1175/1520-0469(1996)053<0497:RPICCA>2.0.CO;2, 1996.

Schaefer, V. J.: The Production of Ice Crystals in a Cloud of Supercooled Water Droplets, Science, 104, 457–459, https://doi.org/10.1126/science.104.2707.457, 1946.

Schmale, J., Henning, S., Decesari, S., Henzing, B., Keskinen, H., Sellegri, K., Ovadnevaite, J., Pöhlker, M. L., Brito, J., Bougiatioti, A., Kristensson, A., Kalivitis, N., Stavroulas, I., Carbone, S., Jefferson, A., Park, M., Schlag, P., Iwamoto, Y., Aalto, P., Äijälä, M., Bukowiecki, N., Ehn, M., Frank, G., Fröhlich, R., Frumau, A., Herrmann, E., Herrmann, H., Holzinger, R., Kos, G., Kulmala, M., Mihalopoulos, N., Nenes, A., O'Dowd, C., Petäjä, T., Picard, D., Pöhlker, C., Pöschl, U., Poulain, L., Prévôt, A. S. H., Swietlicki, E., Andreae, M. O., Artaxo, P., Wiedensohler, A., Ogren, J., Matsuki, A., Yum, S. S., Stratmann, F., Baltensperger, U., and Gysel, M.: Long-Term Cloud Condensation Nuclei Number Concentration, Particle Number Size Distribution and Chemical Composition Measurements at Regionally Representative Observatories, Atmospheric Chemistry and Physics, 18, 2853–2881, https://doi.org/10.5194/acp-18-2853-2018, 2018.

Schmidli, J., Böing, S., and Fuhrer, O.: Accuracy of Simulated Diurnal Valley Winds in the Swiss Alps: Influence of Grid Resolution, Topography Filtering, and Land Surface Datasets, Atmosphere, 9, 196, https://doi.org/10.3390/atmos9050196, 2018.

Seifert, A. and Beheng, K. D.: A Two-Moment Cloud Microphysics Parameterization for Mixed-Phase Clouds. Part 1: Model Description, Meteorology and Atmospheric Physics, 92, 45–66, https://doi.org/10.1007/s00703-005-0112-4, 2006.

Sin'kevich, A. A., Boe, B., Mikhailovskii, Yu. P., Dovgalyuk, Yu. A., Veremei, N. E., Gopalakrishnan, V., Murugavel, P., and Pawar, S. D.: Investigation of Cu Cong Seeding Effect during Rainfall Augmentation in India, Russian Meteorology and Hydrology, 43, 209–217, https://doi.org/10.3103/S1068373918040015, 2018.

Smagorinsky, J.: GENERAL CIRCULATION EXPERIMENTS WITH THE PRIMITIVE EQUATIONS: I. THE BASIC EXPERIMENT, Monthly Weather Review, 91, 99–164, https://doi.org/10.1175/1520-0493(1963)091<0099:GCEWTP>2.3.CO;2, 1963.

Storelvmo, T. and Tan, I.: The Wegener-Bergeron-Findeisen Process – Its Discovery and Vital Importance for Weather and Climate, Meteorologische Zeitschrift, pp. 455–461, https://doi.org/10.1127/metz/2015/0626, 2015.

Tessendorf, S. A., French, J. R., Friedrich, K., Geerts, B., Rauber, R. M., Rasmussen, R. M., Xue, L., Ikeda, K., Blestrud, D. R., Kunkel, M. L., Parkinson, S., Snider, J. R., Aikins, J., Faber, S., Majewski, A., Grasmick, C., Bergmaier, P. T., Janiszeski, A., Springer, A., Weeks, C., Serke, D. J., and Bruintjes, R.: A Transformational Approach to Winter Orographic Weather Modification Research: The SNOWIE Project, Bulletin of the American Meteorological Society, 100, 71–92, https://doi.org/10.1175/BAMS-D-17-0152.1, 2019.

Touloupas, G., Lauber, A., Henneberger, J., Beck, A., and Lucchi, A.: A convolutional neural network for classifying cloud particles recorded by imaging probes, Atmospheric Measurement Techniques, 13, 2219–2239, https://doi.org/10.5194/amt-13-2219-2020, 2020.

Vonnegut, B.: The Nucleation of Ice Formation by Silver Iodide, Journal of Applied Physics, 18, 593–595, https://doi.org/10.1063/1.1697813, 1947.

Wang, W., Yao, Z., Guo, J., Tan, C., Jia, S., Zhao, W., Zhang, P., and Gao, L.: The Extra-Area Effect in 71 Cloud Seeding Operations during Winters of 2008–14 over Jiangxi Province, East China, Journal of Meteorological Research, 33, 528–539, https://doi.org/10.1007/s13351-019-8122-1, 2019.

Wegener, A.: Thermodynamik der Atmosphäre, Barth, 1911.

Woodley, W. L., Rosenfeld, D., and Silverman, B. A.: Results of On-Top Glaciogenic Cloud Seeding in Thailand. Part I: The Demonstration Experiment, Journal of Applied Meteorology and Climatology, 42, 920–938, https://doi.org/10.1175/1520-0450(2003)042<0920:ROOGCS>2.0.CO;2, 2003.

Xie, S., Boyle, J., Klein, S. A., Liu, X., and Ghan, S.: Simulations of Arctic Mixed-Phase Clouds in Forecasts with CAM3 and AM2 for M-PACE, Journal of Geophysical Research: Atmospheres, 113, https://doi.org/10.1029/2007JD009225, 2008.

Xue, L., Hashimoto, A., Murakami, M., Rasmussen, R., Tessendorf, S. A., Breed, D., Parkinson, S., Holbrook, P., and Blestrud, D.: Implementation of a Silver Iodide Cloud-Seeding Parameterization in WRF. Part I: Model Description and Idealized 2D Sensitivity Tests, Journal of Applied Meteorology and Climatology, 52, 1433–1457, https://doi.org/10.1175/JAMC-D-12-0148.1, 2013a.

Xue, L., Tessendorf, S. A., Nelson, E., Rasmussen, R., Breed, D., Parkinson, S., Holbrook, P., and Blestrud, D.: Implementation of a Silver Iodide Cloud-Seeding Parameterization in WRF. Part II: 3D Simulations of Actual Seeding Events and Sensitivity Tests, Journal of Applied Meteorology and Climatology, 52, 1458–1476, https://doi.org/10.1175/JAMC-D-12-0149.1, 2013b.

Xue, L., Chu, X., Rasmussen, R., Breed, D., and Geerts, B.: A Case Study of Radar Observations and WRF LES Simulations of the Impact of Ground-Based Glaciogenic Seeding on Orographic Clouds and Precipitation. Part II: AgI Dispersion and Seeding Signals simulated by WRF, Journal of Applied Meteorology and Climatology, 55, 445–464, https://doi.org/10.1175/JAMC-D-15-0115.1, 2016.

Xue, L., Weeks, C., Chen, S., Tessendorf, S. A., Rasmussen, R. M., Ikeda, K., Kosovic, B., Behringer, D., French, J. R., Friedrich, K., Zaremba, T. J., Rauber, R. M., Lackner, C. P., Geerts, B., Blestrud, D., Kunkel, M., Dawson, N., and Parkinson, S.: Comparison between

https://doi.org/10.5194/egusphere-2023-3029
Preprint. Discussion started: 18 January 2024

Observed and Simulated AgI Seeding Impacts in a Well-Observed Case from the SNOWIE Field Program, Journal of Applied Meteorology and Climatology, 61, 345–367, https://doi.org/10.1175/JAMC-D-21-0103.1, 2022.

Yang, H.-Y., Chang, K.-H., Chae, S., Jung, E., Seo, S., Jeong, J.-Y., Lee, J.-H., Ro, Y., and Kim, B.-J.: Case Study of Ground-Based Glaciogenic Seeding of Clouds over the Pyeongchang Region, Advances in Meteorology, 2018, e9465 923, https://doi.org/10.1155/2018/9465923, 2018.

Zängl, G., Reinert, D., Rípodas, P., and Baldauf, M.: The ICON (ICOsahedral Non-hydrostatic) Modelling Framework of DWD and MPI-M: Description of the Non-Hydrostatic Dynamical Core, Quarterly Journal of the Royal Meteorological Society, 141, 563–579, https://doi.org/10.1002/qj.2378, 2015.

Ćurić, M., Janc, D., and Vučković, V.: Cloud seeding impact on precipitation as revealed by cloud-resolving mesoscale model, Meteorology and Atmospheric Physics, 95, 179–193, https://doi.org/10.1007/s00703-006-0202-y, 2007.